Accurate quantification of brown adipose tissue mass by xenon-enhanced computed tomography

Rosa T. Branca[a,b,1], Andrew McCallister[a,b], Hong Yuan[b,c], Amir Aghajanian[d], James E. Faber[d], Nicholas Weimer[a], Riley Buchanan[a], Carlos S. Floyd[a], Michael Antonacci[a,b], Le Zhang[b,e], and Alex Burant[a,b]

[a]Department of Physics and Astronomy, University of North Carolina at Chapel Hill, Chapel Hill, NC 27599; [b]Biomedical Research Imaging Center, University of North Carolina at Chapel Hill, Chapel Hill, NC 27599; [c]Department of Radiology, University of North Carolina at Chapel Hill, Chapel Hill, NC 27599; [d]Department of Cell Biology and Physiology, University of North Carolina at Chapel Hill, Chapel Hill, NC 27599; and [e]Department of Applied Physical Sciences, University of North Carolina at Chapel Hill, Chapel Hill, NC 27599

Detection and quantification of brown adipose tissue (BAT) mass remains a major challenge, as current tomographic imaging techniques are either nonspecific or lack the necessary resolution to quantify BAT mass, especially in obese phenotypes, in which this tissue may be present but inactive. Here, we report quantification of BAT mass by xenon-enhanced computed tomography. We show that, during stimulation of BAT thermogenesis, the lipophilic gas xenon preferentially accumulates in BAT, leading to a radiodensity enhancement comparable to that seen in the lungs. This enhancement is mediated by a selective reduction in BAT vascular resistance, which greatly increases vascular perfusion of BAT. This enhancement enables precise identification and quantification of BAT mass not only in lean, but also in obese, mouse phenotypes, in which this tissue is invisible to conventional tomographic imaging techniques. The method is developed and validated in rodents and then applied in macaques to assess its feasibility in larger species.

brown adipose tissue | xenon-enhanced CT | FDG-PET | brown adipose tissue mass | xenon

In purely energetic terms, obesity results from an imbalance between energy intake and energy expenditure. Ways to increase energy expenditure include exercise and activation of brown adipose tissue (BAT). BAT is a fat tissue specialized in nonshivering thermogenesis (NST), a process that could increase energy expenditure by as much as 600 kCal per 100 g/d (1, 2). However, the precise contribution of activated BAT to daily energy expenditure in humans is still a contentious issue, as the total mass of this tissue is unknown. To date, there is no acceptable gold standard, aside from histology, for the detection of BAT mass (3–5). While positron emission tomography with fluorodeoxyglucose (^{18}F-FDG-PET) used in conjunction with computed tomography (CT) has been instrumental in advancing our understanding of BAT (6–9), this methodology cannot correctly quantify BAT mass (4, 10). First, ^{18}F-FDG-PET/CT indirectly reports only on BAT activity, not mass, preventing accurate quantification of this tissue in lean individuals, as well as overweight or obese individuals wherein activity may be reduced or absent (11, 12). Second, because glucose uptake in BAT is dissociated from heat production (10) and confounded by many factors, including cold adaptation, feeding status, insulin, and glucose plasma level, quantification of BAT mass based on ^{18}F-FDG standardized uptake values (SUVs) can lead to either overestimation or underestimation of BAT mass (6, 13). Hence, by relying on ^{18}F-FDG-PET/CT measurements of BAT mass, it is not surprising that some have suggested an irrelevant contribution (1–2%) of this tissue to daily energy expenditure (14) because of its paucity, while others have estimated a sizable contribution (5–20%) based on larger estimates of BAT mass (7, 15).

In addition to ^{18}F-FDG-PET/CT, other imaging techniques, including MRI (16) and noncontrast CT (17), have been proposed as alternatives to quantify BAT volume. Here, detection and quantification of BAT mass is often based on measurements of tissue hydration (16, 18). However, such measurements can be very misleading, as BAT hydration exhibits high intersubject and intrasubject variability (19). In addition, in obese phenotypes (20, 21), BAT hydration is similar to that of white adipose tissue (WAT), preventing its differentiation and detection.

A key requirement to quantify the total contribution of this tissue to human energy expenditure and to understand how this tissue develops, grows, and changes in humans throughout a lifetime or under different environmental and metabolic conditions is the availability of a noninvasive imaging technique that can accurately measure its mass in the general adult population, including obese subjects—the treatment population for novel BAT-targeted anti-obesity therapies—in which this tissue may be present but inactive.

Recently, we demonstrated that the lipophilic and inert gas xenon could be used as a MRI probe to detect the presence of BAT in both lean and obese mice (21). Despite xenon showing a strong affinity for BAT during adrenergic stimulation of NST, the quenching of nuclear spin polarization during vascular delivery of this contrast agent hampers the acquisition of high-resolution maps required to accurately quantify BAT volume (21).*

Because of its high Z number, xenon is also an excellent contrast agent for CT. For several decades, the gas has been used to measure lung ventilation function and brain perfusion in humans

Significance

The search for new obesity drug targets and the rediscovery of active brown fat (brown adipose tissue; BAT) in adult humans has triggered a BAT renaissance. However, the assumption that this tissue plays a key role in energy balance in humans, as it does in rodents, is still a matter of debate. This is because BAT mass cannot be correctly quantified by current imaging techniques, as these are either nonspecific or lack the necessary sensitivity to detect BAT, especially in obese phenotypes. Here, we show that xenon-enhanced computed tomography can accurately quantify BAT mass, especially in obese mouse phenotypes in which extensive BAT hypertrophy hampers the detection of this tissue by current tomographic imaging techniques.

(22, 23). Upon inhalation, xenon diffuses from the alveoli to blood, which transports the inert atoms to other tissues. Since extravascular tissue radiodensity increases linearly with the local xenon concentration, quantification of tissue enhancement during xenon inhalation can provide a direct and accurate measurement of xenon concentration and distribution in tissues.

In this work, we first assessed the affinity of xenon for BAT by performing xenon-enhanced CT (XECT) studies in rodents, before and during adrenergic stimulation of BAT. We then evaluated the possibility of using xenon gas as a CT contrast agent to detect and quantify BAT, independently of its thermogenic capacity or hydration status, in lean and obese animal models, in which current imaging techniques failed to detect this tissue. By modeling xenon gas uptake in tissues and by performing tissue microangiography, we then determined the conditions that lead to enhanced xenon uptake in BAT during stimulation of thermogenesis. Finally, we assessed the feasibility of such a methodology in nonhuman primates (NHPs).

Such an approach has clinical relevance, as it can provide complimentary information on BAT mass that is indispensable for understanding how this tissue evolves over time and for correctly quantifying its true contribution to whole-body energy expenditure.

Results

Xenon Biodistribution Measurements. To evaluate the specificity of xenon to BAT, we first assessed xenon biodistribution in vivo by performing CT studies on lean and obese (ob/ob) mouse models, in which current tomographic imaging techniques typically fail to detect this tissue.

For these studies, mice were mechanically ventilated with either a mixture of nitrogen and oxygen (nonenhanced scan) or a mixture of xenon and oxygen (enhanced scan). Enhanced scans were performed before and after stimulation of NST in BAT, achieved by a s.c. injection of norepinephrine. Tissue enhancement was then quantified by measuring the change in tissue radiodensity on precontrast and postcontrast images. During the same imaging session, half of the animals also underwent an ^{18}F-FDG-PET/CT scan.

Fig. 1A shows measured average radiodensity enhancement and xenon concentration in different tissues in lean and obese mice before and during stimulation of NST. As expected, before stimulation of NST (NST$^-$), the brain showed the highest enhancement, followed by the liver, muscle, and BAT. The average liver radiodensity enhancement at baseline was significantly higher ($P < 0.02$, $n = 12$, homoscedastic t test) in obese mice than in lean mice, consistent with the higher liver fat content in these animals. BAT radiodensity enhancement at baseline was similar in lean and obese mice and comparable to that observed in muscle, while WAT radiodensity enhancement was quite low in both lean and obese mice. During stimulation of NST (NST$^+$), no significant ($P > 0.05$, $n = 12$, paired t test) increase in tissue radiodensity was observed in the brain, liver, WAT, or muscle. However, a significant ($P \leq 2E-7$, $n = 12$, paired t test) increase in BAT radiodensity of >150 Hounsfield units (HU) was observed during stimulation of NST (NST$^+$) in both phenotypes. Interestingly, in obese mice, the magnitude of the enhancement was similar to that in lean mice.

Detection and Quantification of BAT Mass by XECT. Based on enhancement calibration measurements (Fig. S1), the strong increase in BAT radiodensity during stimulation of NST corresponded to an in-tissue xenon concentration of a few tens of millimolar, a concentration that has never been reported for distal organs in mice during xenon inhalation. As a result, while before stimulation of NST (NST$^-$), BAT radiodensity was considerably lower than that of surrounding muscle (Fig. 1 B and C), during stimulation (NST$^+$), the strong increase in BAT radiodensity made this tissue suddenly visible in CT images. Surprisingly, BAT enhancement during NST was also remarkable in the
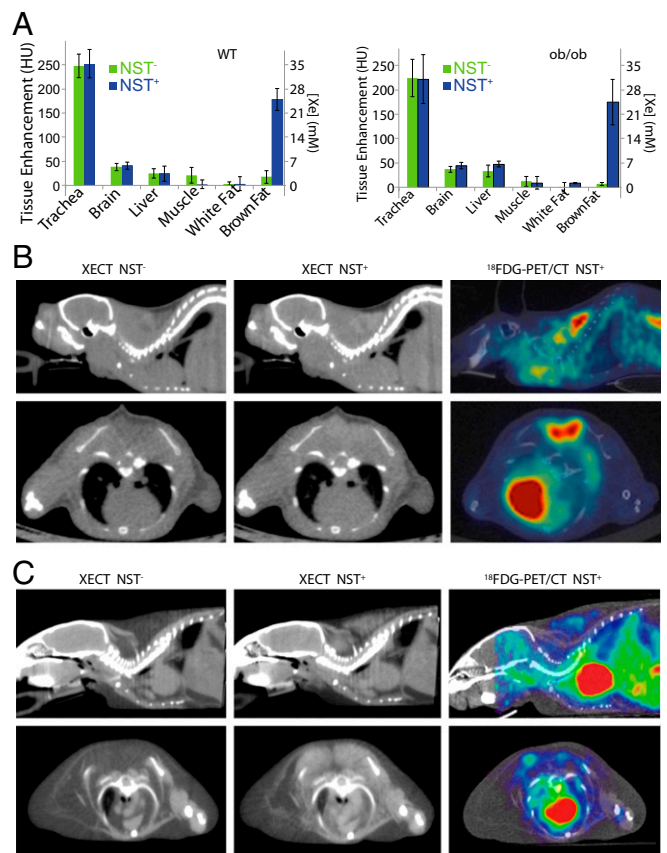
Fig. 1. Xenon radiodensity enhancement during stimulation of NST enables BAT detection in lean and obese mouse phenotypes. (A) Enhancement in Hounsfield units (HU) and calculated xenon concentration in millimolar, as measured for six different tissues before (NST$^-$; green) and during (NST$^+$; blue) stimulation of NST in lean and obese mice. Error bars represent SD for $n = 12$ mice. (B) Representative sagittal (Upper) and axial (Lower) XECT and ^{18}F-FDG-PET/CT images acquired in a lean mouse before (NST$^-$) and during (NST$^+$) stimulation of NST. (C) Representative sagittal (Lower) XECT and ^{18}F-FDG-PET/CT images acquired in an obese mouse before (NST$^-$) and during (NST$^+$) stimulation of NST. Images shown are representative of XECT images collected in $n = 12$ lean and $n = 12$ obese animals and of ^{18}F-FDG-PET/CT images collected in $n = 6$ lean and $n = 6$ obese mice.
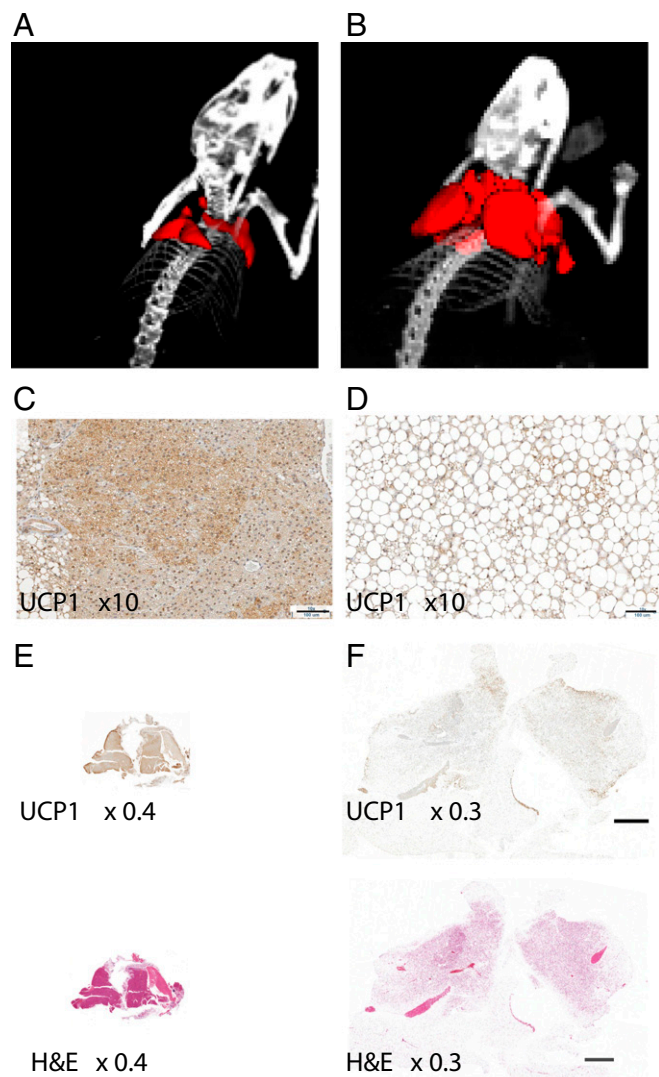
obese phenotype (Fig. 1C), in which BAT fat content was similar to that of surrounding WAT, making this tissue indistinguishable from WAT in noncontrast CT images and in contrast CT images acquired before adrenergic stimulation.

Comparison with ^{18}F-FDG-PET/CT Scans. Despite a BAT radiodensity enhancement >150 HU being observed during NST$^+$ in all lean and obese mice analyzed, ^{18}F-FDG-PET/CT scans showed that four (SUV$_{mean}$ ± SD of 1.2 ± 0.3; SUV$_{max}$ ± SD of 1.7 ± 0.4) of the six lean mice and only one (SUV$_{mean}$ ± SD of 2.1 ± 0.4; SUV$_{max}$ ± SD of 2.9 ± 0.9) of the six obese mice analyzed had a BAT glucose uptake >1 SUV. In all other mice, the average SUV$_{mean}$ value was 0.4 ± 0.1, with a SUV$_{max}$ of 0.9 ± 0.06, significantly higher ($P < 0.00005$, $n = 6$, homoscedastic t test) than SUV values in surrounding WAT (0.13 ± 0.11, $n = 6$, homoscedastic t test), but not significantly different ($P > 0.5$) than that in muscle (SUV$_{mean}$ ± SD of 0.3 ± 0.2, $n = 6$, homoscedastic t test). More importantly, in all mice with a BAT glucose uptake >1 SUV, spillover and partial volume effects led to a Dice correlation coefficient between XECT and ^{18}F-FDG-PET/CT BAT mass <0.6.

MEDICAL SCIENCES

The 3D-Volumetric Measurement of BAT. Fig. 2 shows representative 3D-volumetric renderings of BAT as obtained by XECT datasets in both lean (Fig. 2*A*) and obese (Fig. 2*B*) mice. As is clear from the map, XECT was able to identify and quantify all BAT depots in the mouse upper thorax: the interscapular, axillary, and cervical depots. These depots were clearly present in both phenotypes. However, a significant difference ($P < 5E\text{-}06$,

for homoscedastic t test and $P < 0.0001$ for heteroscedastic t test, $n = 12$) in BAT volume was found between the two phenotypes. While the average BAT volume was 175 ± 50 mm^3 (mean $\pm$ SD, $n = 12$) in lean mice, an average BAT volume of 800 ± 150 mm^3 (mean $\pm$ SD, $n = 12$) was found in obese mice, confirming the extensive hypertrophy of this tissue found histologically (Fig. 2 *C–F*).

Histological and Immunohistochemistry Analyses. Histological and immunohistochemistry analyses, which were performed to identify the nature of the tissue that underwent radiodensity enhancement during NST$^+$, showed that the enhanced tissue always contained Uncoupling Protein 1$^+$ (UCP1$^+$) adipocytes (Fig. 2 *C–F*). However, while in lean mice, the enhanced tissue presented the characteristic morphological features of BAT, with highly hydrated multilocular adipocytes with a strong UCP1 content (Fig. 2 *C* and *E*), in obese mice, the enhanced tissue appeared to be very heterogeneous: A core containing multilocular adipocytes with greater UCP1 content was surrounded by a periphery containing UCP1$^+$ adipocytes with a single large lipid droplet in the cytoplasm, morphologically resembling beige adipocytes (Fig. 2 *D* and *F*). In this phenotype, the increased food intake, coupled with a positive energy balance (25), led to an increase in lipid droplet size and BAT hypertrophy.

Modeling of Xenon Uptake in Tissues. Next, we sought to understand how, in the lean and obese mouse phenotypes, the reported difference in blood flow enhancement during NST$^+$ (25) led to a similar BAT radiodensity enhancement. By using the Kety–Smith equation (26) (*Supporting Information*) and by using reported tissue blood flow and tissue/blood partition coefficients values for brain and BAT (25, 27, 28), we quantified the expected time dependence of xenon concentration in BAT of lean and obese mice. As shown in Fig. 3*A*, in brain tissue, given the relatively low tissue/blood partition coefficient and large blood flow, saturation was already reached at baseline during the first few minutes of xenon inhalation. Therefore, stimulation of NST does not lead to a significant enhancement in brain radiodensity. On the other hand, given the relatively large tissue/blood partition coefficient and low blood flow at baseline, BAT was far from becoming saturated during the first 4 min of xenon inhalation. However, during NST$^+$, the increase in blood flow to this tissue reduced wash-in time, leading to an increase in xenon uptake. More importantly, based on this model, the magnitude of the increase in xenon uptake and tissue radiodensity seen in BAT during NST$^+$ depended not only on the increase in blood flow, but also on the solubility of xenon into the tissue. As a result, even when the increase in BAT tissue blood flow is not very large, a large enhancement can be obtained if the solubility of xenon in the tissue is quite large, as in obese animals.

Microangiography of BAT Reveals Changes in Vasculature Resistance and Tissue Perfusion in Lean Mice During Norepinephrine Infusion. To understand how norepinephrine infusion, which we used to stimulate NST, impacted BAT perfusion and thus xenon uptake, we performed arterial casting of interscapular BAT in control mice and in mice pretreated with norepinephrine. Microfil, with a viscosity adjusted to impede capillary transit (8:1 silicone-to-diluent), was infused retrograde via the aorta. Light microscopy was then used to assess differences in vascular density in treated and control mice after the excised tissue had been optically cleared. Fig. 3 shows arteriograms from a control (Fig. 3*B*) and a norepinephrine-treated (Fig. 3*C*) lean mouse. In control mice, collaterals (arterial–arterial anastomoses labeled with red asterisks in Fig. 3*B*) were evident between the circulations supplying the BAT and WAT masses. These collaterals, together with high vascular resistance in BAT, diverted perfusion to the surrounding WAT such that little or no filling was seen within
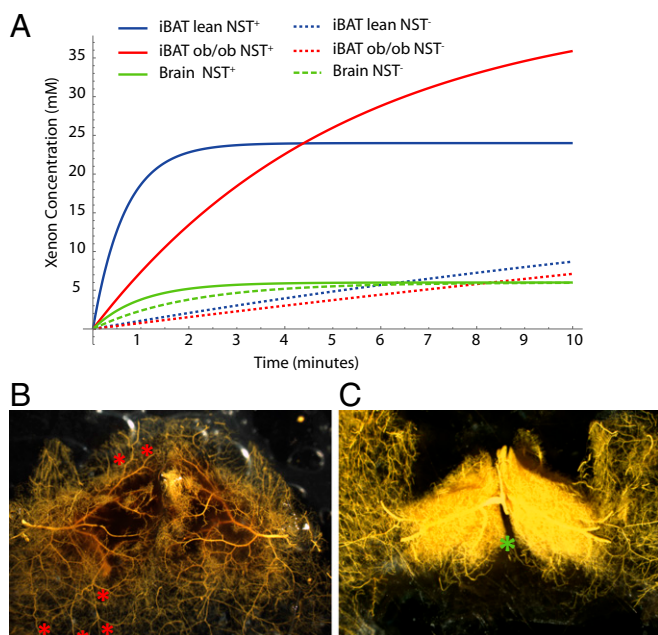

Fig. 2. The 3D volumetric rendering of BAT by XECT and histology reveal extensive BAT hypertrophy in the obese mouse phenotype. (*A*) Representative 3D volumetric map of interscapular and cervical BAT as detected by XECT in lean mice. Several depots are visible: deep cervical portion, superficial cervical, interscapular, subscapular, and axillo-thoracic, as reported by Vitali et al. (39) and Frontini and Cinti (40). Image shown is representative of 3D volumetric maps collected in $n = 12$ lean mice. (*B*) Representative 3D volumetric rendering of interscapular and cervical BAT as detected by XECT in an ob/ob mouse. Image shown is representative of 3D volumetric maps collected in $n = 12$ obese mice. (*C*) High-magnification (10×) image of 5-μm UCP1-stained section of interscapular BAT from the same lean mouse. (Scale bar: 100 μm.) (*D*) High-magnification (10×) image of 5-μm UCP1-stained section of interscapular BAT from the same obese mouse. (Scale bar: 100 μm.) (*E*) Low-magnification (4×) images of 5-μm UCP1-stained section and hematoxylin–eosin-stained section of interscapular BAT from the same lean mouse. (*F*) Low-magnification (0.3×) image of 5-μm hematoxylin–eosin- and UCP1-stained section of interscapular BAT from the same obese mouse. Histological sections shown here are representative of interscapular BAT sections as collected from $n = 6$ lean mice and $n = 6$ obese mice.

Fig. 3. BAT microangiography reveals norepinephrine-induced changes in vasculature resistance during NST. (*A*) Modeling of xenon concentration in BAT and brain before and during stimulation of NST. (*B*) High-magnification (10×) of the vasculature of interscapular BAT (poorly filled region) and surrounding WAT (well-perfused region) of a control mouse perfused with the vasodilator nitroprusside and filled with yellow Microfil. At baseline, resistance to blood flow in BAT is increased with respect to surrounding WAT such that BAT is less perfused than surrounding WAT. Arterial–arterial anastomoses (collaterals; red asterisks) can be seen, which provide a low-resistance connection between BAT arteries and WAT artery trees/territories, shunting blood to WAT. (*C*) High-magnification (10×) of the vasculature of interscapular BAT of a mouse treated with norepinephrine before filling with yellow Microfil. During adrenergic stimulation of NST with norepinephrine, blood flow through BAT is increased dramatically. The increase can be ascribed to local vasoactive actions of norepinephrine that, by reducing vascular resistance in BAT and increasing the resistance of the collaterals, shunts blood from WAT to BAT. As a result, in response to sympathetic stimulation during cold exposure, simulated by norepinephrine treatment, resistance to blood flow in surrounding WAT increases, and blood flow is shunted to BAT. The differential response to sympathetic stimulation in BAT vs. WAT suggests that the BAT vascular bed is unique in its adrenergic signaling for control of the resistance of its vessels and collaterals. Images shown are representative of $n = 5$ control and $n = 6$ norepinephrine-treated mice. The location of the Sultzer's vein is indicated by a green asterisk.

the Sultzer's vein (labeled with a green asterisk in Fig. 3*C*), the main vein that drains blood flow from BAT. In contrast, as is evident in the representative angiograms, treatment with norepinephrine induced a remarkable increase in BAT perfusion.

Quantification of BAT in NHPs. To assess the feasibility of XECT detection of BAT volume in larger species, the protocol was tested in two adult 10-y-old female rhesus monkeys. In rhesus monkeys, the anatomical distribution and macroscopic appearance of BAT is similar to that in humans. In these animals, as in adult humans, BAT is not found in the interscapular region, but is found primarily in the cervical and axillary region (29, 30). Microscopically, the tissue resembles that of obese mice, with brown adipocytes slightly larger and with fewer lipid droplets (31). For these studies, the NHPs were anesthetized and intubated for XECT scans. Following a baseline CT scan, a mixture of <40 vol % xenon/60 vol % oxygen was inhaled for 8 min, and CT scans were performed right before the end of the inhalation procedure. Two XECT scans were performed: one before and one during norepinephrine infusions. The ^{18}F-FDG-

PET/CT scans were acquired during the same imaging session for comparison. Fig. 4*A* shows average radiodensity enhancement obtained in the two animals in different tissues before (NST$^-$) and during (NST$^+$) stimulation of NST. After segmenting out all major visible blood vessels, a significant enhancement of >30 HU (P < 3E-04, $n = 10$, paired t test) was observed in glucose-avid fat tissues located in the supraclavicular fat pocket and in the axillary region. No significant enhancement was observed between NST$^-$ and NST$^+$ scans in muscle ($P > 0.8$, $n = 10$, paired t test) or WAT ($P > 0.07$, $n = 10$, paired t test). Fig. 4*B* shows BAT volumetric maps in the two NHPs as obtained by using ^{18}F-FDG-PET/CT and XECT. The ^{18}F-FDG-PET/CT maps were constructed by using a SUV threshold of 0.75 since ^{18}F-FDG uptake in supraclavicular BAT, although higher than surrounding muscle and white fat, was consistently <1.5 SUV in NHP-1 (Table 1). Consistent with mouse results, despite the two methodologies being able to detect BAT depots in similar locations, the measured Dice similarity coefficient was only 40%.

Discussion

After >8 y of renewed interest in BAT, the functional relevance of BAT in humans is still largely undetermined, as estimations of BAT volume have ranged from a meager 14 g (14) to >500 g (5, 7, 13). Accurate quantification of BAT mass still presents major challenges, especially in obese subjects, where the need is greatest and where detection of BAT mass could potentially shift the focus from interventions that aim at augmenting the mass of this tissue to interventions that aim at stimulating the activity of this tissue.

The inability to correctly quantify BAT is common not only to imaging techniques, such as ^{18}F-FDG-PET, that base their detection on tissue activity, but also to other imaging techniques, such as CT or MRI, that aim at detecting BAT based on its morphological features. In principle, CT and MRI can both differentiate the more hydrated BAT from the less hydrated WAT, even in the absence of tissue activation, based on differences in tissue radiodensity or fat content. However, since tissue fat fraction is not a marker of BAT (4), in practice, this is possible only in lean mice and newborn babies (16, 32), where BAT is chronically stimulated and tissue hydration is remarkably different from in WAT. In obese mice or obese humans, BAT fat content can be much higher (19, 33), making differentiation of BAT from WAT a challenge. As a result, when these techniques are applied in humans, only a lower fat-fraction threshold (typically 30–40%) is used to identify BAT in the supraclavicular fat depot, leading to inclusion of WAT, with which BAT is often mixed, and considerable overestimation of tissue mass (34, 35).

Our results unequivocally demonstrate that xenon is both specific as well as sensitive to BAT. Upon xenon inhalation, stimulation of BAT thermogenesis, which may or may not be followed by BAT activation (26, 36), led to an increase in xenon uptake by BAT and enhanced the radiodensity of this tissue by >150 HU, regardless of tissue glucose uptake. This radiodensity enhancement is comparable only to that seen in the lungs and much higher than what has been observed in any other tissue. This enhancement, as confirmed by the inert gas model and BAT microangiography, was the result of an increase in blood flow, which is specific to BAT (25), but also decoupled from BAT activity (36).

Microangiography of BAT in lean mice revealed that this increase in blood flow to BAT was mediated by a change in vasculature resistance. Specifically, under basal conditions, patent arterial–arterial shunts partially diverted arterial blood into the surrounding WAT at a precapillary level, effectively reducing xenon uptake in BAT. During stimulation of NST, exogenous or endogenous noradrenaline released from sympathetic nerve terminals reduced or eliminated shunting. As a result, a greater fraction of the arterial blood supply, and thus a greater fraction of xenon,
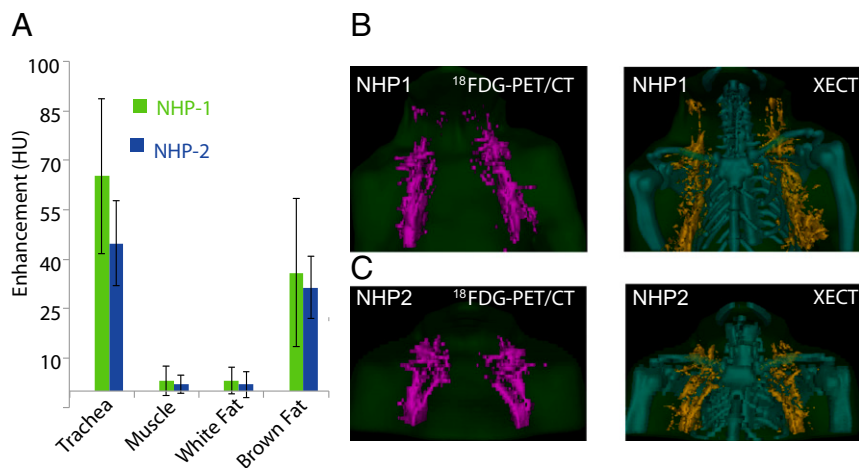
Fig. 4. Xenon radiodensity enhancement during stimulation of NST enables 3D BAT volume quantification in NHPs. (*A*) Average radiodensity enhancement measured from selected regions of interest, before and during stimulation of NST, as measured in NHPs (*n* = 2). Error bars represent SD. (*B*) The 3D volumetric map of BAT as obtained by combined ^{18}F-FDG-PET/CT and XECT in one of the NHPs (NHP1). (*C*) The 3D volumetric map of BAT as obtained by combined ^{18}F-FDG-PET/CT and by XECT in the other NHP (NHP2).

was able to reach the parenchymal capillary bed and diffuse into the tissue, leading to a reduction of the xenon wash-in rate and to an overall increase in tissue uptake. However, it is important to specify that, although the enhancement was a consequence of the increase in tissue blood flow, the magnitude of the enhancement was not directly proportional to the increase in tissue blood flow. In the obese phenotype, for example, despite the much smaller increase in blood flow to BAT during adrenergic stimulation, we observed a BAT enhancement similar to that seen in lean mice. Based on the xenon gas uptake model, the lipid-rich BAT of obese phenotypes represents a better host for the lipophilic gas xenon, such that even a reduced increase in tissue blood flow was able to lead to a comparable increase in tissue radiodensity. As such, the sensitivity of XECT to BAT is expected to be much higher than the sensitivity of other imaging modalities that try to identify this tissue based solely on changes in tissue blood flow.

Despite the limited number of studies performed in NHPs, performed solely to assess the feasibility of this imaging modality in larger species by using a clinical CT scanner, these studies nicely mimicked our mouse results. In NHPs, despite glucose uptake in BAT being different between the two animals, a similar increase in tissue radiodensity was observed in the supraclavicular fat pad during norepinephrine infusion. In NHPs, consistent with what was previously found histologically in this species (37), XECT scans revealed discrete BAT pockets within the glucose avid supraclavicular fat tissue, located mainly near major blood vessels. BAT volumes measured in the two animals were also comparable. On the other hand, BAT volume measured by ^{18}F-FDG-PET/CT scans strongly depended on the SUV threshold used. The ^{18}F-FDG-PET/CT measurements of BAT volume, by relying on volumetric measurements of tissue activity, produced variable results based on the tissue's level of activity and on the capacity of the tissue to take up glucose during activation. More importantly, when directly compared with XECT and histology, partial volume effect and spillover in ^{18}F-FDG-PET/CT images led to either overestimation or underestimation of BAT mass.

Compared with hyperpolarized xenon gas MRI (HPXEMRI) detection of BAT, the major advantage of XECT is clearly its higher resolution. While with HPXEMRI, BAT maps can be acquired with a spatial resolution <2 cm^3 in mice, and much lower in humans, XECT provides BAT maps with a significantly better spatial resolution, both in mice and NHPs, enabling the detection and differentiation of all BAT depots that have been histologically found and reported in the literature. This resolution is clearly needed to be able to correctly quantify the mass of this tissue that, as in NHPs, is found around major blood vessels or mixed with WAT. In addition, unlike HPXEMRI, this technique does not require the use of special equipment for gas hyperpolarization, but can be implemented by using commercial CT scanners. The major disadvantage is, of course, the radiation dose associated with CT scans that, although similar to the radiation dose associated with ^{18}F-FDG-PET/CT scans, may prevent the use of this technique for repetitive scans. The other major disadvantage is the need for a continuous xenon-inhalation protocol, which, given the anesthetic properties of xenon, will be required to achieve a detectable change in tissue radiodensity while keeping xenon concentration <30%. Nonetheless, there are no fundamental barriers to rapid translation of this methodology to clinical research and perhaps clinical care, as XECT has and is currently being used for lung ventilation studies in humans. However, while for lung ventilation function, XECT and HPXEMRI are often seen as competing modalities, here, they should be seen as complementary: While XECT can provide maps of BAT with a resolution needed to accurately quantify this tissue, HPXEMRI can provide important complementary information on BAT thermogenic function that cannot be obtained otherwise.

In summary, we demonstrated how the radiodense gas xenon can be used in CT scans to accurately measure BAT volume. The lipophilic gas appears to be an ideal probe for BAT that, when used in CT scans, can lead to an accurate identification and quantification of this tissue, regardless of its thermogenic or glucose uptake capacity. As such, XECT can provide the necessary tool to accurately quantify the volume of this tissue and to monitor changes

Table 1. ^{18}F-FDG-PET/CT and XECT BAT values in NHP

NHP	^{18}F-FDG-PET/CT BAT volume ± SD, mL	SUV$_{max}$	SUV$_{mean}$ ± SD	XECT BAT volume ± SD, mL	BAT enhancement, HU, mean ± SD	Dice
NHP-1	18.12 ± 1 (SUV> 0.75)	1.6	0.87 ± 0.11	9.9 ± 1	36 ± 22	0.4
NHP-2	13.9 ± 1 (SUV > 0.75)	4.57	2.45 ± 0.77	6.4 ± 1	31 ± 9	0.52

The table reports total BAT volume as measured by combined ^{18}F-FDG-PET/CT and as measured by XECT. The table also reports SUV$_{max}$, SUV$_{mean}$, mean XECT enhancement across the entire BAT volume, along with the Dice correlation coefficient between ^{18}F-FDG-PET/CT maps and XECT maps of BAT.

in tissue morphology under different stimuli and interventions. More interestingly, these measurements of BAT volumes can be easily integrated with current functional PET/CT measurements of tissue activity that are commonly used for BAT studies in humans, or with functional measurement of tissue thermogenic activity by HPXEMRI, to provide complementary morphological information on this tissue.

Materials and Methods

Mouse Studies. All animal experiments were performed under an approved animal protocol and according to the guidelines from the Institutional Animal Care and Use Committee (IACUC) at the University of North Carolina at Chapel Hill, and conducted in compliance with the NIH's *Guide for the Care and Use of Laboratory Animals* (38). A total of 12 fasted C57BL/6J and 12 B6. V-*Lep^{ob}* (ob/ob) mice, anesthetized with pentobarbital, underwent a XECT imaging protocol consisting of a nonenhanced CT scan and two enhanced CT scans, performed before and after the injection of norepinephrine. During the same imaging session, half of the mice (six lean and six ob/ob) also underwent an 18F-FDG-PET scan. For these scans, 10 min after norepinephrine injection and right before the second XECT scan, animals were injected with 18F-FDG. PET images were then acquired after the acquisition of the last XECT images and 1 h after radiotracer injection. In 12 of the 24 animals imaged, tissue was dissected right after imaging and prepared for immunohistochemistry analysis.

NHP Studies. XECT and 18F-FDG-PET studies were performed on two female rhesus macaques under propofol anesthesia, on a hybrid human PET/CT system (Biograph mCT; Siemens Healthcare). XECT scans were acquired right after an 8-min continuous inhalation protocol of 40 vol % xenon in oxygen, before and after the beginning of norepinephrine infusion. Approximately

20 min from the beginning of norepinephrine infusion, 18F-FDG was injected i.v., and static PET images were acquired 1 h later.

Image Analysis. Quantification of radiodensity enhancement in phantoms and mice was performed by using OsiriX software (Pixmeo SARL), whereas NHP images were analyzed by using MIM (MIM Software Inc.). In NHP, BAT was identified as fat tissue that underwent an increase in radiodensity during norepinephrine infusion >20 HU. In 18F-FDG-PET/CT images, BAT was identified as a tissue with an HU between −100 and −50 HU and with an SUV > 0.75, since SUVs in NHP-1 were well below 1.5 SUV.

Statistical Analysis. The sample size for mouse studies was based on the number of mice necessary to quantify average enhancement in BAT and other tissues. This sample size confers to our study a power >95% at a two-sided alpha level of 0.05.

The sample size for NHPs was dictated by the availability of only two NHPs at our institution. By using a paired *t* test and considering a mean enhancement in BAT of 20 HU and a SD of 10 HU, the use of $n = 2$ NHPs is expected to confer to our study a power of 80%, at a two-sided alpha level of 0.05.

For statistical significance testing, we used two-sided homoscedastic *t* tests with a significance level of type I error set at 0.05 for rejecting the null hypothesis. Heteroscedastic *t* test and paired-sample *t* tests were used where indicated. Tests for data normality were performed by using the Shapiro–Wilk test with a significance level >0.05.

Additional and more detailed information on materials and methods can be found in *Supporting Information*.

1. Cannon B, Nedergaard J (2004) Brown adipose tissue: Function and physiological significance. *Physiol Rev* 84:277–359.
2. Cannon B, Nedergaard J (1985) The biochemistry of an inefficient tissue: Brown adipose tissue. *Essays Biochem* 20:110–164.
3. Sampath SC, Bredella MA, Cypess AM, Torriani M (2016) Imaging of brown adipose tissue: State of the art. *Radiology* 280:4–19.
4. Cypess AM, Haft CR, Laughlin MR, Hu HH (2014) Brown fat in humans: Consensus points and experimental guidelines. *Cell Metab* 20:408–415.
5. Leitner BP, et al. (2017) Mapping of human brown adipose tissue in lean and obese young men. *Proc Natl Acad Sci USA* 114:8649–8654.
6. Orava J, et al. (2011) Different metabolic responses of human brown adipose tissue to activation by cold and insulin. *Cell Metab* 14:272–279.
7. Ouellet V, et al. (2012) Brown adipose tissue oxidative metabolism contributes to energy expenditure during acute cold exposure in humans. *J Clin Invest* 122:545–552.
8. van der Lans AA, et al. (2013) Cold acclimation recruits human brown fat and increases nonshivering thermogenesis. *J Clin Invest* 123:3395–3403.
9. Ouellet V, et al. (2011) Outdoor temperature, age, sex, body mass index, and diabetic status determine the prevalence, mass, and glucose-uptake activity of 18F-FDG-detected BAT in humans. *J Clin Endocrinol Metab* 96:192–199.
10. Hankir MK, et al. (2017) Dissociation between brown adipose tissue 18 F-FDG uptake and thermogenesis in uncoupling protein 1 deficient mice. *J Nucl Med* 58:1100–1103.
11. Vijgen GHEJ, et al. (2011) Brown adipose tissue in morbidly obese subjects. *PLoS One* 6:e17247.
12. Vijgen GHEJ, et al. (2012) Increase in brown adipose tissue activity after weight loss in morbidly obese subjects. *J Clin Endocrinol Metab* 97:E1229–E1233.
13. van der Lans AAJJ, et al. (2014) Cold-activated brown adipose tissue in human adults: Methodological issues. *Am J Physiol Regul Integr Comp Physiol* 307:R103–R113.
14. Muzik O, et al. (2013) 15O PET measurement of blood flow and oxygen consumption in cold-activated human brown fat. *J Nucl Med* 54:523–531.
15. van Marken Lichtenbelt WD, Schrauwen P (2011) Implications of nonshivering thermogenesis for energy balance regulation in humans. *Am J Physiol Regul Integr Comp Physiol* 301:R285–R296.
16. Hu HH, Smith DL, Jr, Nayak KS, Goran MI, Nagy TR (2010) Identification of brown adipose tissue in mice with fat-water IDEAL-MRI. *J Magn Reson Imaging* 31:1195–1202.
17. Lubura M, et al. (2012) Non-invasive quantification of white and brown adipose tissues and liver fat content by computed tomography in mice. *PLoS One* 7:e37026.
18. Baba S, Jacene HA, Engles JM, Honda H, Wahl RL (2010) CT Hounsfield units of brown adipose tissue increase with activation: Preclinical and clinical studies. *J Nucl Med* 51:246–250.
19. Heaton JM (1972) The distribution of brown adipose tissue in the human. *J Anat* 112:35–39.
20. Branca RT, et al. (2013) In vivo noninvasive detection of brown adipose tissue through intermolecular zero-quantum MRI. *PLoS One* 8:e74206.
21. Branca RT, et al. (2014) Detection of brown adipose tissue and thermogenic activity in mice by hyperpolarized xenon MRI. *Proc Natl Acad Sci USA* 111:18001–18006.
22. Bouma GJ, et al. (1992) Ultra-early evaluation of regional cerebral blood flow in severely head-injured patients using xenon-enhanced computerized tomography. *J Neurosurg* 77:360–368.
23. Good WF, Gur D (1991) Xenon-enhanced CT of the brain: Effect of flow activation on derived cerebral blood flow measurements. *AJNR Am J Neuroradiol* 12:83–85.
24. Breslow MJ, et al. (1999) Effect of leptin deficiency on metabolic rate in ob/ob mice. *Am J Physiol* 276:E443–E449.
25. Thurlby PL, Trayhurn P (1980) Regional blood flow in genetically obese (ob/ob) mice. The importance of brown adipose tissue to the reduced energy expenditure on non-shivering thermogenesis. *Pflugers Arch* 385:193–201.
26. Kety SS (1951) The theory and applications of the exchange of inert gas at the lungs and tissues. *Pharmacol Rev* 3:1–41.
27. Foster DO, Frydman ML (1979) Tissue distribution of cold-induced thermogenesis in conscious warm- or cold-acclimated rats reevaluated from changes in tissue blood flow: The dominant role of brown adipose tissue in the replacement of shivering by nonshivering thermogenesis. *Can J Physiol Pharmacol* 57:257–270.
28. Wickler SJ, Horwitz BA, Stern JS (1986) Blood flow to brown fat in lean and obese adrenalectomized Zucker rats. *Am J Physiol* 251:R851–R858.
29. Swick AG, Kemnitz JW, Houser WD, Swick RW (1986) Norepinephrine stimulates activity of brown adipose tissue in rhesus monkeys. *Int J Obes* 10:241–244.
30. Walston J, et al. (1997) The β3-adrenergic receptor in the obesity and diabetes prone rhesus monkey is very similar to human and contains arginine at codon 64. *Gene* 188:207–213.
31. Sheldon EF (1924) The so-called hibernating gland in mammals: A form of adipose tissue. *Anat Rec* 28:331–347.
32. Hu HH, Tovar JP, Pavlova Z, Smith ML, Gilsanz V (2012) Unequivocal identification of brown adipose tissue in a human infant. *J Magn Reson Imaging* 35:938–942.
33. Deng J, et al. (August 11, 2017) MRI characterization of brown adipose tissue under thermal challenges in normal weight, overweight, and obese young men. *J Magn Reson Imaging*, 10.1002/jmri.25836.
34. McCallister A, Zhang L, Burant A, Katz L, Branca RT (2017) A pilot study on the correlation between fat fraction values and glucose uptake values in supraclavicular fat by simultaneous PET/MRI. *Magn Reson Med* 78:1922–1932.
35. van Rooijen BD, et al. (2013) Imaging cold-activated brown adipose tissue using dynamic T2*-weighted magnetic resonance imaging and 2-deoxy-2-[18F]fluoro-D-glucose positron emission tomography. *Invest Radiol* 48:708–714.
36. Abreu-Vieira G, Hagberg CE, Spalding KL, Cannon B, Nedergaard J (2015) Adrenergically-stimulated blood flow in brown adipose tissue is not dependent on thermogenesis. *Am J Physiol Endocrinol Metab* 308:E822–E829.
37. Chaffee RRJ, et al. (1975) Studies on thermogenesis in brown adipose tissue in temperature-acclimated Macaca mulatta. *Comp Biochem Physiol A* 50:303–306.
38. National Research Council (2011) *Guide for the Care and Use of Laboratory Animals* (National Academies Press, Washington, DC), 8th Ed.
39. Vitali A, et al. (2012) The adipose organ of obesity-prone C57BL/6J mice is composed of mixed white and brown adipocytes. *J Lipid Res* 53:619–629.
40. Frontini A, Cinti S (2010) Distribution and development of brown adipocytes in the murine and human adipose organ. *Cell Metab* 11:253–256.

MEDICAL SCIENCES